Editors' Suggestion   Featured in Physics

Topological Metric Detects Hidden Order in Disordered Media

Dominic J. Skinner[,1] Boya Song,[1] Hannah Jeckel,[2,3] Eric Jelli,[2,3] Knut Drescher,[2,3] and Jörn Dunkel[1]

[1]*Department of Mathematics, Massachusetts Institute of Technology, Cambridge, Massachusetts 02139-4307, USA*
[2]*Max Planck Institute for Terrestrial Microbiology, 35043 Marburg, Germany*
[3]*Department of Physics, Philipps-Universität Marburg, 35043 Marburg, Germany*

Recent advances in microscopy techniques make it possible to study the growth, dynamics, and response of complex biophysical systems at single-cell resolution, from bacterial communities to tissues and organoids. In contrast to ordered crystals, it is less obvious how one can reliably distinguish two amorphous yet structurally different cellular materials. Here, we introduce a topological earth mover's (TEM) distance between disordered structures that compares local graph neighborhoods of the microscopic cell-centroid networks. Leveraging structural information contained in the neighborhood motif distributions, the TEM metric allows an interpretable reconstruction of equilibrium and nonequilibrium phase spaces and embedded pathways from static system snapshots alone. Applied to cell-resolution imaging data, the framework recovers time ordering without prior knowledge about the underlying dynamics, revealing that fly wing development solves a topological optimal transport problem. Extending our topological analysis to bacterial swarms, we find a universal neighborhood size distribution consistent with a Tracy-Widom law.

Discrete particulate objects, from atoms to cells, compose the majority of physical and living systems. Modern microscopy and simulation techniques enable us to study the elementary building blocks of solids [1,2], colloidal and granular materials [3–5], bacterial biofilms [6,7], and tissues [8] with unprecedented resolution over large scales. These experimental and computational advances have highlighted the importance of local spatial organization [9] and disorder [10] for the global behaviors of both equilibrium and nonequilibrium materials, spurring substantial theoretical efforts to link discrete microstructure with macroscale properties. Prime examples include the recent successful characterizations of epithelial cell (EC) layers and other cellular materials through the geometric [11,12] and topological [13–16] analysis of Voronoi and Delaunay tessellations [17]. In spite of such major progress, high-resolution data continue to pose fundamental conceptual and practical challenges regarding the proper classification of discrete physical and biological structures. Specifically, it is still unclear whether one can recover parametric embeddings, phase space dimensions, and time ordering from a topological analysis of static snapshots alone and whether such analysis can help reveal the governing principles of multicellular development.

To tackle these problems, we introduce here a topological earth mover's (TEM) distance by combining ideas from statistical topology [13–15,18,19] and optimal transport theory [20,21] with nonequilibrium statistical mechanics [22]. The TEM metric compares two discrete material structures by quantifying the statistical differences in the local network topology of their Delaunay triangulations (Fig. 1). Unlike purely entropic measures, the TEM framework leverages information contained in the energetic distances between different network topologies, enabling a finer distinction and classification. Intuitively, computing $\text{TEM}(A, B)$ amounts to estimating the smallest number of edge flips needed to make the local network topology of material A statistically indistinguishable from the local network topology of material B. Physically, this procedure can be interpreted as finding the average lowest-energy path connecting two disordered structures, and we provide an efficient algorithm for realizing this computationally demanding task for systems with $\sim 10^6$ particles [23].

To demonstrate the practical potential of this framework for the analysis of both equilibrium and nonequilibrium systems, we present a broad set of applications: First, we show that the TEM metric successfully distinguishes jammed disordered packings of both mono- and polydisperse ellipsoids. Thereafter, we use the TEM framework to reconstruct the nonequilibrium phase diagram of active Brownian particle (ABP) simulations without recourse to time-resolved data. Next, by measuring the pairwise TEM distances between unsorted experimental images of a developing fruit fly wing, we are able to reconstruct their temporal ordering and discover that wing development follows an optimal transport geodesic, suggesting a previously unrecognized optimization principle in tissue development. Finally, by extending our topological analysis to single-cell-resolution data from bacterial swarming experiments, we observe a universal
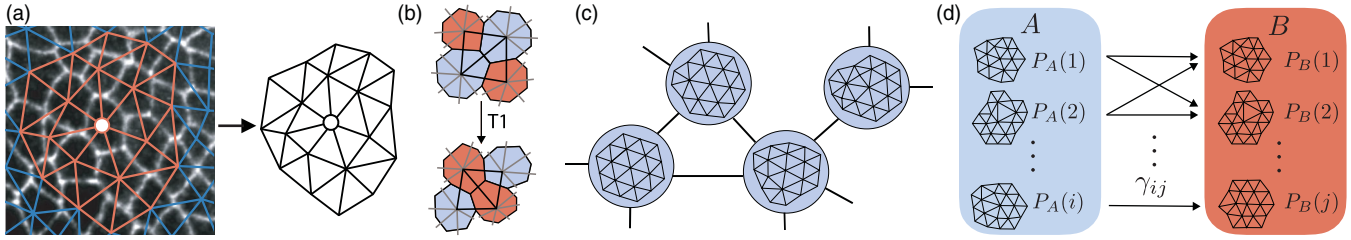
FIG. 1. Key conceptual steps for calculating the TEM distance illustrated for an epithelial cell layer. (a) Experimental image of epithelial cell layer from *Drosophila* embryo (adapted with permission from Refs. [8,37]) with Delaunay triangulation overlayed (blue, red). The local neighborhood network of radius $r = 2$ (red) is shown for a selected vertex (white circle). (b) A topological $T1$ transition, corresponding to an exchange of neighbors, is reflected in a change of the local radius-2 neighborhood. Voronoi cells (red, blue) with Delaunay triangulation overlayed (black, gray) are shown. (c) Nodes of the flip graph correspond to networks and are connected by an edge if the networks are one $T1$ transition (or flip) away from each other. (d) The map γ_{ij} transports the neighborhood motif distribution of material A to the motif distribution of material B.

neighborhood size distribution consistent with a Tracy-Widom law.

To define the TEM distance, we consider the specific example of a two-dimensional (2D) cell layer as shown in Fig. 1(a), although all subsequent definitions generalize to arbitrary point sets in $\mathbb{R}^2$ or $\mathbb{R}^3$. Our starting point is the Delaunay triangulation [17] of the cell-centroid positions as shown in Fig. 1(a). In practice, it is often sufficient to take the positions of the EC nuclei as vertices of the Delaunay network [38]. If two random realizations of such networks are generated by the same physical or biological process, they will have different vertex positions and topology, but their local statistical properties (local connectivity patterns, etc.) will be identical, provided the networks are sufficiently large. This fact has been exploited previously to define entropic [14] and earth movers' distances between cell complexes [15], as well as to classify structure in amorphous materials [39]. Here, we extend these ideas to define a physically motivated topological metric that measures statistical differences in the local Delaunay triangulations around vertices. Specifically, we define for each vertex a local neighborhood of radius r, which consists of all the vertices that are not more than r edges away from the central vertex [see red subgraph corresponding to $r = 2$ in Fig. 1(a)]. Taking $r = 1$ typically results in only $O(10)$ distinguishable neighborhood motifs, severely constraining possible forms of the motif distribution [23]. By contrast, we found that $r = 2$, which increases the range of observable motifs to $O(10^4)$, suffices for many practical applications [23]. Although r can, in principle, be chosen arbitrarily large, TEM computations become expensive for larger neighborhoods $r \geq 3$; we therefore focus on the case $r = 2$ from now on. The local neighborhoods of two vertices are of the same topological type i if they are graph isomorphic. Counting the occurrences of the various neighborhood types i across all vertices yields a probability distribution $P(i) \geq 0$ that characterizes the topostatistical state of the cell network.

To provide an intuitive physical motivation for the TEM metric, we note that a nondegenerate Delaunay network is invariant under infinitesimal perturbations and can change only through a topological $T1$ transition [Fig. 1(b)]. For EC layers there is an energy barrier to $T1$ transitions [40], and so the energy cost to transform from one neighborhood type to another is directly related to the number of $T1$ transitions required. For other packed systems, there typically exist similar energetic costs for changing neighbors through $T1$ transitions. Motivated by this, we can define the energetic distance between two neighborhoods as the minimum number of $T1$ transitions separating them. This mathematically well-defined metric [23,41] induces naturally a secondary graph structure, known as the flip graph [24], where nodes correspond to neighborhood types i and are linked with an edge if they are one $T1$ transition away from each other [Fig. 1(c)]. The minimum path length between two nodes on the flip graph is the smallest number of $T1$ transitions needed to move between the corresponding neighborhood types. Moreover, the distribution $P(i)$ of neighborhood types in the EC layer can now be viewed as a distribution on the nodes i of the flip graph [blue box in Fig. 1(d)].

Armed with this intuition, we can now define the TEM distance between the Delaunay triangulations of two materials A and B in a natural manner as the earth mover's or, equivalently, Wasserstein distance [20] between their neighborhood distributions P_A and P_B over the flip graph: If $P_A(i)$ is the probability of neighborhood i occurring in material A, and $P_B(j)$ is the probability of neighborhood j occurring in material B, then a transport map, $\gamma_{ij} \geq 0$, from A to B satisfies $\sum_j \gamma_{ij} = P_A(i)$, $\sum_i \gamma_{ij} = P_B(j)$, see Fig. 1(d). Then, the TEM distance between A and B is

$$\text{TEM}(A, B) = \min_{\gamma} \sum_{ij} \gamma_{ij} d(i, j), \qquad (1)$$

where $d(i, j)$ is the distance between the neighborhoods i and j on the flip graph, and the minimum is taken over all possible transport maps $\gamma = (\gamma_{ij})$. We emphasize that, in contrast to widely used entropic distance measures between distributions [14], the definition of TEM uses the physically relevant information encoded in the metric structure $d(i, j)$ of the underlying observable space, which in our case reflects the typical energy cost of a $T1$ transition between network motifs. As a consequence, TEM generally outperforms purely entropic Kullback-Leibler and Jensen-Shannon divergences when one needs to distinguish complex structures that are characterized by weakly overlapping distributions; see Ref. [25] and the Supplemental Material [23] for explicit examples.

For large systems, the minimization problem (1) becomes computationally challenging. We combined two algorithmic insights [23] to calculate TEM efficiently for disordered materials with millions of particles. After computation of the Delaunay tessellation, which can be done with high parallel efficiency [42], we utilize a modification of the Weinberg algorithm [23,26] to determine the flip-graph distances $d(i, j)$ of N observed neighborhood motifs in $O(N)$ steps. Given $d(i, j)$, the minimization over the transport maps $\{\gamma_{ij}\}$ can be recast as an minimum cost flow problem [20,23], which is efficiently solved with linear programming [43]. To demonstrate the broad applicability of our TEM framework, we focus in the remainder of this Letter on applications relevant to current major research areas: colloidal packings, collective far-from-equilibrium dynamics, tissue development, and spatiotemporally heterogeneous multicellular systems.

Recent advances in the fabrication of geometrically complex colloids [3,4] and imaging techniques [6] have led to a renewed practical and theoretical interest in the characterization of granular [5,44] and biological materials [6,7]. Of particular importance in this context

are the often fundamentally different behaviors of monodisperse [45] and polydisperse [46] colloidal systems. While the former are much better understood theoretically, the latter are often practically more relevant to natural systems and processes, such as particle segregation seen in industrial agriculture, cereals, or avalanches [47]. To demonstrate the usefulness of the TEM framework for capturing the essential topostatistical differences between and across mono- and polydisperse systems, we generated jammed disordered packings of 10 000 ellipsoids using an event-driven packing code [48]. Specifically, we were interested in distinguishing two different pathways for transitioning from a monodisperse packing of spheres (ellipsoids with aspect ratio 1∶1) to a monodisperse packing of ellipsoids with aspect ratio 1∶3 [Fig. 2(a)]. The first "monodisperse" transition path was realized by simulating 12 monodisperse packings of ellipsoids with aspect ratios varying from 1∶1 to 1∶3 [bottom path in Fig. 2(a)]. The second "polydisperse" transition path was realized by simulating 12 different binary mixtures of 1∶1 and 1∶3 ellipsoids [top path in Fig. 2(a)]. Computing the TEM distances between all 24×24 pairs of simulations produces the symmetric TEM distance matrix shown in Fig. 2(b). Given this matrix, it is natural to seek a faithful low-dimensional embedding in Euclidean space $\mathbb{R}^d$ that approximately preserves the TEM distance structure. To construct the embedding we choose multidimensional scaling (MDS), a generalized principal component (PC) analysis based on the TEM distance [49]. Since each pathway corresponds to a 1D manifold (as only one parameter is varied in each case), the phase space can be embedded in $\mathbb{R}^2$; indeed, the $\mathbb{R}^2$ embedding clearly distinguishes the two different pathways [Fig. 2(c)]. To find the dimensionality of the phase space, we calculate the residual variance that plateaus at the relevant dimension [23,28] and correctly identifies the ellipsoid embedding as 2D [Fig. 2(d)]. We show in the
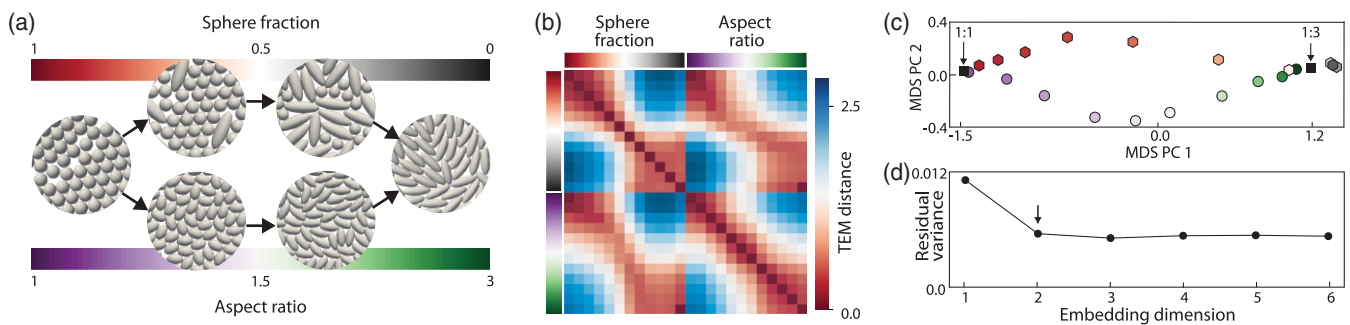

FIG. 2. Two-dimensional poly- and monodisperse packings are distinguished by the TEM distance. (a) Two alternative paths from aspect ratio 1∶1 to aspect ratio 1∶3 ellipsoid packings. Top is monodisperse with varying aspect ratios; bottom is polydisperse with a mixture of 1∶1 and 1∶3 aspect ratios. (b) Distance matrix where each pixel represents the pairwise distance between simulated 2D planar ellipsoid packings, each containing 10 000 ellipsoids. (c) Simulations are embedded in 2D using MDS, recovering two distinct paths, one for monodisperse simulations (hexagons) and one for polydisperse simulations (circles). (d) The residual variance plateaus after embedding dimension 2, correctly identifying the true embedding dimension of the phase space (arrow).
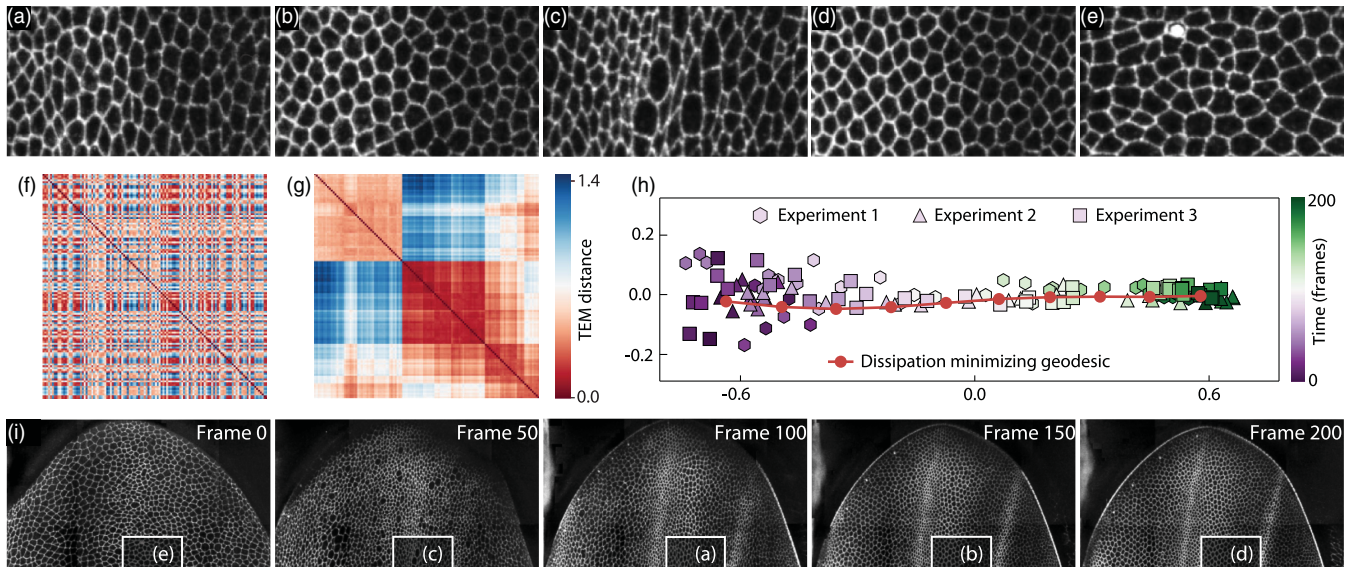
FIG. 3.   Developing *Drosophila* embryos solve topological optimal transport problem, with MDS embedding recovering temporal order. (a)–(e) Enlarged images showing epithelial cells at unknown times. Three experiments and 40 time frames per experiment were used. (f) Matrix of TEM distances between unsorted experimental images has no apparent structure. (g) TEM distance matrix sorted by hierarchical clustering shows approximately three phases. (h) 2D MDS embedding recovers the temporal order as the principal component. Included in the embedding are intermediate stages of a dissipation-minimizing [23] geodesic between average start and end states, which the data fall on. (i) The correct temporal ordering of the image time series is recovered. The white boxes show the source of images (a)–(e). Data adapted with permission from Refs. [8,37].

Supplemental Material [23] that the same approach can be used to infer the nonequilibrium phase space of ABP simulations [29] from instantaneous system configurations. More broadly, these examples illustrate how the TEM metric can discover phase spaces from configurational snapshots alone.

In the remainder, we show that the topological analysis of data from two recent experiments [8,27] can reveal previously unrecognized biophysical optimization principles and universal statistical signatures. We begin by considering shuffled images [Figs. 3(a)–3(e)] of developing fruit fly embryo wings [8,37]. Using the Delaunay triangulation of the cell centroids, hierarchical clustering [50] of the TEM distance matrix of the shuffled images [Fig. 3(f)] reveals three developmental main phases [Fig. 3(g)]. The resulting MDS embedding is essentially 1D, with the first principal component corresponding to time [Fig. 3(h)], and thus restores the temporal order of the data [Fig. 3(i)]. This shows how the TEM framework can be used to infer temporal ordering from ensemble measurements [51]. More importantly, however, the TEM analysis reveals the developmental trajectory of the fly wing follows a topological geodesic, a continuous curve that minimizes the total length with respect to the TEM distance. While earth movers' geodesics are in general not unique, a unique path can be found by additionally minimizing transport dissipation [21,23]. The data fluctuate closely around this minimum-dissipation geodesic [red curve in Fig. 3(h)], meaning that fly wing development approximately solves

a dissipation-constrained topological optimal transport problem.

Finally, we provide a more detailed characterization of the neighborhood motif distributions in 2D nonequilibrium systems. To this end, we analyze recent bacterial swarming experiments [27] using machine learning [23] to identify individual cells [Figs. 4(a) and 4(b)]. By determining the motif size distributions for snapshots taken at different space-time locations in a growing swarm, we find that both mean and variance vary systematically with space, time, and cell density [Figs. 4(c)–4(e)]. Strikingly, after rescaling to zero mean and unit variance, the combined motif size distribution closely matches [23] a universal Tracy-Widom (TW) distribution [Fig. 4(f)]. TW distributions were recently reported for growing fluctuating fronts [52], dynamics of self-assembly [53], active particle dynamics [54,55], and phase transitions between strongly and weakly coupling regimes [56]. We also find TW motif size distributions in the ABP and fly wing data when subsampling from the liquid like phase [23], suggesting that TW distributions play a central role in the topostatistics of amorphous and nonequilbrium systems.

To conclude, the TEM metric framework will be broadly applicable, from single-cell RNA sequencing [57], cryo-lectron microscopy [58], and organoid characterization [59] to structural transitions in living [6,11] and nonliving [3] matter. In particular, it enables a direct comparison of the topological statistical properties of a wide range of fundamentally different systems, the only requirement being that
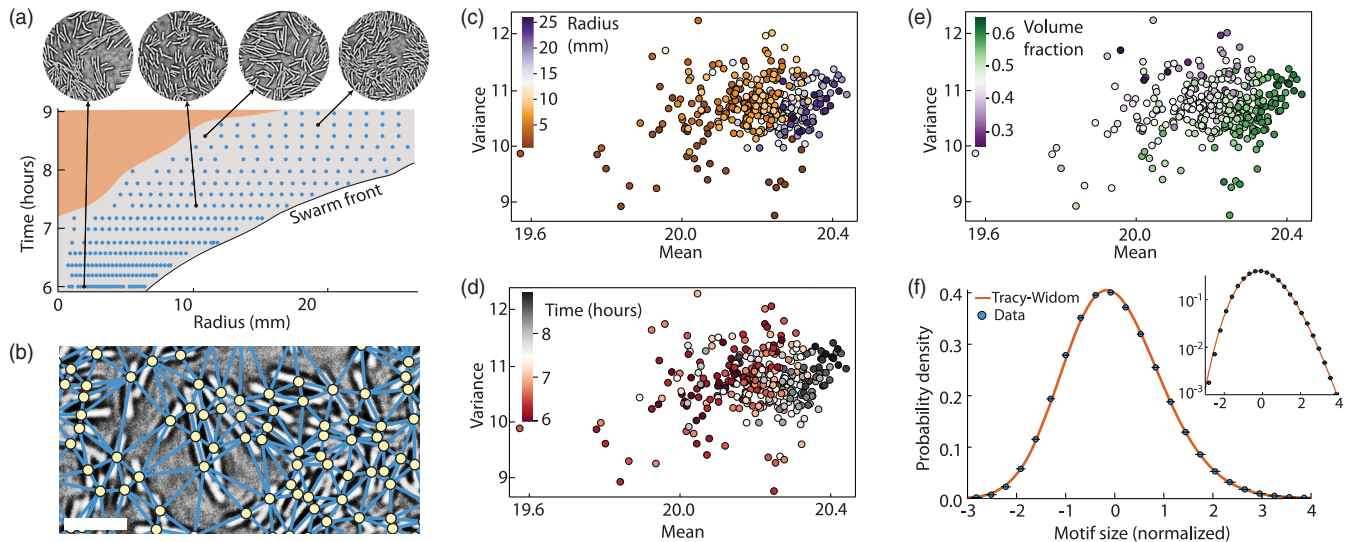
FIG. 4. Motif sizes in heterogenous bacterial swarms exhibit universal nonequilibrium statistics. (a) An azimuthally symmetric bacterial swarm expands as motile cells grow and divide [27]. We analyzed configurational snapshots at different space-time positions in the swarming monolayer phase (blue dots; select example images at the top); the central multilayered biofilm phase (red) was excluded. (b) Aided by a machine learning algorithm, cell centroids (yellow circles) and their Delaunay tessellation (blue lines) were determined. Scale bar: 10 μm. (c)–(e) The distribution of motif sizes, defined as the number of vertices per $r = 2$ neighborhood, is heterogenous in space and time. The mean motif size increases, on average, with radial distance and time (c),(d). The variance decreases with area filling fraction (e), reflecting more ordered cell packings in dense swarming regions. (f) After normalizing to zero mean and unit variance, the combined histogram over all space-time snapshots (circles) follows a universal Tracy-Widom distribution (line). Horizontal error bars represent the standard deviation within a bin. Inset: log scale plot.

transitions between basic motifs (Delaunay neighborhood structures, DNA strings, etc.) can be mapped onto a joint flip-graph structure.

[1] G. Binnig and H. Rohrer, Rev. Mod. Phys. **59**, 615 (1987).
[2] Y. Sugimoto, P. Pou, M. Abe, P. Jelinek, R. Pérez, S. Morita, and Ó. Custance, Nature (London) **446**, 64 (2007).
[3] S. C. Glotzer and M. J. Solomon, Nat. Mater. **6**, 557 (2007).
[4] V. Soni, E. Bililign, S. Magkiriadou, S. Sacanna, D. Bartolo, M. Shelley, and W. Irvine, Nat. Phys. **15**, 1188 (2019).
[5] S. Nauer, L. Böttcher, and M. A. Porter, J. Complex Netw., https://doi.org/10.1093/comnet/cnz037 (2019).
[6] R. Hartmann, P. Singh, P. Pearce, R. Mok, B. Song, F. Díaz-Pascual, J. Dunkel, and K. Drescher, Nat. Phys. **15**, 251 (2019).
[7] D. Dell'Arciprete, M. Blow, A. Brown, F. Farrell, J. Lintuvuori, A. McVey, D. Marenduzzo, and W. Poon, Nat. Commun. **9**, 4190 (2018).
[8] R. Etournay, M. Popović, M. Merkel, A. Nandi, C. Blasse, B. Aigouy, H. Brandl, G. Myers, G. Salbreux, F. Jülicher, and S. Eaton, eLife **4**, e07090 (2015).
[9] P. Pearce, B. Song, D. J. Skinner, R. Mok, R. Hartmann, P. K. Singh, H. Jeckel, J. S. Oishi, K. Drescher, and J. Dunkel, Phys. Rev. Lett. **123**, 258101 (2019).
[10] C. P. Goodrich, A. J. Liu, and S. R. Nagel, Nat. Phys. **10**, 578 (2014).
[11] D. Bi, X. Yang, M. C. Marchetti, and M. L. Manning, Phys. Rev. X **6**, 021011 (2016).
[12] D. Bi, J. H. Lopez, J. M. Schwarz, and M. L. Manning, Nat. Phys. **11**, 1074 (2015).
[13] E. A. Lazar, J. K. Mason, R. D. MacPherson, and D. J. Srolovitz, Phys. Rev. Lett. **109**, 095505 (2012).
[14] J. K. Mason, E. A. Lazar, R. D. MacPherson, and D. J. Srolovitz, Phys. Rev. E **86**, 051128 (2012).
[15] B. Schweinhart, J. K. Mason, and R. D. MacPherson, Phys. Rev. E **93**, 062111 (2016).
[16] D. Wenzel, S. Praetorius, and A. Voigt, J. Chem. Phys. **150**, 164108 (2019).
[17] F. Aurenhammer, R. Klein, and D.-T. Lee, *Voronoi Diagrams and Delaunay Triangulations*, 1st ed. (World Scientific Publishing Co., River Edge, NJ, 2013).
[18] H. Ronellenfitsch, J. Lasser, D. Daly, and E. Katifori, PLoS Comput. Biol. **11**, e1004680 (2015).
[19] J. W. Rocks, A. J. Liu, and E. Katifori, Phys. Rev. Research **2**, 033234 (2020).
[20] M. Essid and J. Solomon, SIAM J. Sci. Comput. **40**, A1961 (2018).
[21] J. Solomon, R. Rustamov, L. Guibas, and A. Butscher, arXiv:1603.06927.

[22] P. Ronhovde, S. Chakrabarty, D. Hu, M. Sahu, K. K. Sahu, K. F. Kelton, N. A. Mauro, and Z. Nussinov, Sci. Rep. **2,** 329 (2012).

[23] See Supplemental Material at http://link.aps.org/supplemental/10.1103/PhysRevLett.126.048101 for details of derivations, proofs, and experiments, which includes Refs. [8,13,14,17,20,21,24–36].

[24] P. Bose and F. Hurtado, Comput. Geom. **42,** 60 (2009).

[25] J. Solomon, arXiv:1801.07745.

[26] L. Weinberg, IEEE Trans. Circuit Theory **13,** 142 (1966).

[27] H. Jeckel, E. Jelli, R. Hartmann, P. K. Singh, R. Mok, J. F. Totz, L. Vidakovic, B. Eckhardt, J. Dunkel, and K. Drescher, Proc. Natl. Acad. Sci. U.S.A. **116,** 1489 (2019).

[28] J. B. Tenenbaum, V. d. Silva, and J. C. Langford, Science **290,** 2319 (2000).

[29] Y. Fily, S. Henkes, and M. C. Marchetti, Soft Matter **10,** 2132 (2014).

[30] H. Edelsbrunner, D. Kirkpatrick, and R. Seidel, IEEE Trans. Inf. Theory **29,** 551 (1983).

[31] R. A. Wagner and R. Lowrance, J. ACM **22,** 177 (1975).

[32] U. Schmidt, M. Weigert, C. Broaddus, and G. Myers, in *Medical Image Computing and Computer Assisted Intervention—MICCAI 2018*, edited by A. F. Frangi, J. A. Schnabel, C. Davatzikos, C. Alberola-López, and G. Fichtinger (Springer International Publishing, Cham, 2018), pp. 265–273.

[33] O. Ronneberger, P. Fischer, and T. Brox, in *Medical Image Computing and Computer-Assisted Intervention—MICCAI 2015, Lecture Notes in Computer Science* Vol. 9351 (Springer, New York, 2015) [arXiv:1505.04597].

[34] T. J. Yoon, M. Y. Ha, E. A. Lazar, W. B. Lee, and Y.-W. Lee, Phys. Rev. E **100,** 012118 (2019).

[35] E. A. Lazar, J. K. Mason, R. D. MacPherson, and D. J. Srolovitz, Phys. Rev. E **88,** 063309 (2013).

[36] E. Limpert, W. A. Stahel, and M. Abbt, Bio Science **51,** 341 (2001).

[37] R. Etournay, M. Merkel, M. Popović, H. Brandl, N. Dye, B. Aigouy, G. Salbreux, S. Eaton, and F. Jülicher, eLife **5,** e14334 (2016).

[38] R. van Drongelen, T. Vazquez-Faci, T. A. Huijben, M. van der Zee, and T. Idema, J. Theor. Biol. **454,** 182 (2018).

[39] E. A. Lazar, J. Han, and D. J. Srolovitz, Proc. Natl. Acad. Sci. U.S.A. **112,** E5769 (2015).

[40] D. Bi, J. H. Lopez, J. M. Schwarz, and M. L. Manning, Soft Matter **10,** 1885 (2014).

[41] C. L. Lawson, Disc. Math. **3,** 365 (1972).

[42] C. H. Rycroft, Chaos **19,** 041111 (2009).

[43] I. Dunning, J. Huchette, and M. Lubin, SIAM Rev. **59,** 295 (2017).

[44] A. Donev, I. Cisse, D. Sachs, E. A. Variano, F. H. Stillinger, R. Connelly, S. Torquato, and P. M. Chaikin, Science **303,** 990 (2004).

[45] S. Torquato and F. H. Stillinger, Rev. Mod. Phys. **82,** 2633 (2010).

[46] I. S. Aranson and L. S. Tsimring, Rev. Mod. Phys. **78,** 641 (2006).

[47] A. Kudrolli, Rep. Prog. Phys. **67,** 209 (2004).

[48] A. Donev, S. Torquato, and F. H. Stillinger, J. Comput. Phys. **202,** 765 (2005).

[49] I. Borg and P. J. F. Groenen, in *Modern Multidimensional Scaling: Theory and Applications*, 2nd ed. (Springer, New York, 2005), Chap. 12, pp. 201–268.

[50] J. H. Ward, J. Am. Stat. Assoc. **58,** 236 (1963).

[51] P. Pearce, F. G. Woodhouse, A. Forrow, A. Kelly, H. Kusumaatmaja, and J. Dunkel, Nat. Commun. **10,** 5368 (2019).

[52] K. A. Takeuchi, M. Sano, T. Sasamoto, and H. Spohn, Sci. Rep. **1,** 34 (2011).

[53] G. Makey, S. Galioglu, R. Ghaffari, E. D. Engin, G. Yıldırım, Ö. Yavuz, O. Bektaş, Ü. S. Nizam, Ö. Akbulut, Ö. Şahin *et al.*, Nat. Phys. **16,** 795 (2020).

[54] Z. Chen, J. de Gier, I. Hiki, and T. Sasamoto, Phys. Rev. Lett. **120,** 240601 (2018).

[55] C. A. Tracy and H. Widom, Commun. Math. Phys. **290,** 129 (2009).

[56] S. N. Majumdar and G. Schehr, J. Stat. Mech. (2014) P01012.

[57] A. K. Shalek, R. Satija, X. Adiconis, R. S. Gertner, J. T. Gaublomme, R. Raychowdhury, S. Schwartz, N. Yosef, C. Malboeuf, D. Lu *et al.*, Nature (London) **498,** 236 (2013).

[58] N. Fischer, A. L. Konevega, W. Wintermeyer, M. V. Rodnina, and H. Stark, Nature (London) **466,** 329 (2010).

[59] J. F. Dekkers, M. Alieva, L. M. Wellens, H. C. R. Ariese, P. R. Jamieson, A. M. Vonk, G. D. Amatngalim, H. Hu, K. C. Oost, H. J. G. Snippert *et al.*, Nat. Protocols **14,** 1756 (2019).